arXiv:1808.02390v2 [quant-ph] 4 Jun 2019

A spin heat engine coupled to a harmonic-oscillator flywheel

D. von Lindenfels,[1] O. Gräb,[1] C. T. Schmiegelow,[1,*] V. Kaushal,[1] J. Schulz,[1]
Mark T. Mitchison,[2] John Goold,[2] F. Schmidt-Kaler,[1] and U. G. Poschinger[1,†]

[1] *QUANTUM, Institut für Physik, Universität Mainz, Staudingerweg 7, 55128 Mainz, Germany*
[2] *School of Physics, Trinity College Dublin, College Green, Dublin 2, Ireland*

We realize a heat engine using a single electron spin as a working medium. The spin pertains to the valence electron of a trapped $^{40}Ca^{+}$ ion, and heat reservoirs are emulated by controlling the spin polarization via optical pumping. The engine is coupled to the ion's harmonic-oscillator degree of freedom via spin-dependent optical forces. The oscillator stores the work produced by the heat engine and therefore acts as a flywheel. We characterize the state of the flywheel by reconstructing the Husimi $\mathcal{Q}$ function of the oscillator after different engine runtimes. This allows us to infer both the deposited energy and the corresponding fluctuations throughout the onset of operation, starting in the oscillator ground state. In order to understand the energetics of the flywheel, we determine its ergotropy, i.e. the maximum amount of work which can be further extracted from it. Our results demonstrate how the intrinsic fluctuations of a microscopic heat engine fundamentally limit performance.

Heat engines converting thermal energy to mechanical work have always been the centerpiece of thermodynamics. They consist of four fundamental components: a working agent, the cold and hot heat reservoirs, and a mechanism for deposition or extraction of the generated work. Recently, thermal machines have been experimentally demonstrated in the microscopic regime [1–3] and are currently entering the realm of well-controlled atomic systems: A single-ion heat engine [4] and an ion-crystal based refrigerator [5] have been demonstrated recently, and engines based on ensembles of NV centers in diamond [6], superconducting circuits [7] or ensembles of nuclear spins in a NMR setup [8] have been studied. With decreasing size of the constituent parts and at finite operation timescales, well-established notions such as *work*, *heat* and *efficiency* need to be reassessed [9–11]. In particular, far from the thermodynamic limit, fluctuations play a central role [12–14]. For engines comprising a few microscopic degrees of freedom, the impact of quantum effects has been subject to theoretical studies [15–19].

Here, we report on the experimental realization of a heat engine based on a two-level system as a working agent, which is coupled to a harmonic-oscillator degree of freedom [20], where output energy is deposited throughout the operation of the engine. It is henceforth referred to as the *flywheel* [21]. The engine and flywheel degrees of freedom both allow for direct control. This enables the characterization of the energy deposition throughout the onset of the engine operation, at an energy resolution below the single quantum level. Starting with the flywheel initialized in the ground state, we characterize its state after different engine operation times by reconstructing its Husimi $\mathcal{Q}$ function [22]. From this, we infer the energy deposited in the flywheel along with its fluctuations. The measured fluctuations have a significant thermal component, indicating that not all of the energy transferred to the flywheel is extractable work. Therefore, in order to quantify the work done by the engine we evaluate the ergotropy [23–25], i.e., an upper bound on the amount of work which can be extracted from the flywheel. The results reveal how the generation of useful work is limited by effects which are characteristic for microscopic systems.

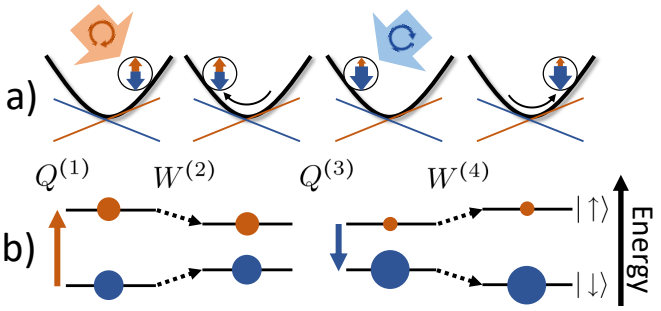


FIG. 1. Operation of the four-stroke engine. **a)** Mechanical picture: The parabolas show the harmonic trap potential and lines indicate the additional spin-dependent optical potential acting on $|\uparrow\rangle$ (red) and $|\downarrow\rangle$ (blue). The arrows within the circles representing the ion correspondingly indicate the spin populations. **b)** Energy representation: The levels indicate the Zeeman energies of $|\uparrow\rangle$ and $|\downarrow\rangle$, and the size of the circles indicates the populations. Shown are the states of the system after each of the engine strokes, from left to right: isochoric heating, isentropic expansion, isochoric cooling and isentropic compression (see text).

Engine operation.—The heat engine operates on the spin of the valence electron pertaining to a single trapped $^{40}Ca^{+}$ ion. The operation is depicted in Fig. 1. Heating and cooling of the spin is achieved by controlling its polarization in an external magnetic field via alternating optical pumping. The harmonic motion of the ion in the confining Paul trap acts as the flywheel. We place the ion in an optical standing wave (SW), which mediates the coupling between the engine and flywheel via a spin-dependent optical dipole force [26, 27] along the oscillation (x) direction. The trap center $x = 0$ coincides with a node of the SW. The Hamiltonian of the coupled

spin-oscillator system reads

$$\hat{H} = \hat{H}_{\mathrm{HO}} + \hbar\left(\omega_z + \Delta_S \sin(k_{\mathrm{SW}}\hat{x})\right)\frac{\hat{\sigma}_z}{2}, \qquad (1)$$

where ω_z denotes the Zeeman splitting of the spin and $\hat{\sigma}_z$ is the Pauli z operator. The bare flywheel Hamiltonian is $\hat{H}_{\mathrm{HO}} = \hbar\omega_t\left(\hat{n}+\frac{1}{2}\right)$, where ω_t is the trap frequency along x and $\hat{n}$ is the number operator. The parameter Δ_S denotes the amplitude of the SW in terms of the spatially varying ac-Stark shift, where $k_{\mathrm{SW}} \approx 2\pi/\ 280$ nm is the effective wavenumber. The internal energy is given by the Zeeman energy of the spin: $U = \hbar\omega_z'(\langle\hat{x}\rangle)\langle\hat{\sigma}_z\rangle/2$. For small displacements $k_{\mathrm{SW}}\langle\hat{x}\rangle \ll 1$, the effective Zeeman shift — the sum of the magnetic field-induced shift and ac Stark shift from the SW — is $\omega_z'(\langle\hat{x}\rangle) = \omega_z + \Delta_S k_{\mathrm{SW}}\langle\hat{x}\rangle$.

Optical pumping with optical polarization alternating at the trap period $2\pi/\omega_t$ emulates the coupling to reservoirs: After each pumping step, the populations of the Zeeman sublevels of the $S_{1/2}$ electronic ground state correspond to a fixed temperature, see Fig. 2 a). The cold reservoir temperature T_C corresponds to predominant population of the lower-energy Zeeman sublevel, i.e. $\langle\hat{\sigma}_z\rangle \gtrsim -1$, while the hot reservoir temperature $T_H > T_C$ corresponds to predominant depolarization, $\langle\hat{\sigma}_z\rangle \lesssim 0$. The hot and cold temperatures are determined via

$$\langle\hat{\sigma}_z\rangle = -\tanh(\hbar\omega_z'/2k_BT). \qquad (2)$$

Close to the the SW node, the ion experiences a mean spin-dependent force $\mathcal{F} = -\hbar k_{\mathrm{SW}}\Delta_S\langle\hat{\sigma}_z\rangle/2$. Since $\langle\hat{\sigma}_z\rangle$ varies periodically at frequency ω_t, this leads to an average resonant driving force on the oscillator, i.e. deposition of work in the flywheel. The engine is equivalent to a four-stroke Otto motor: Associating the effective Zeeman shift ω_z' with the inverse volume of a working gas in a macroscopic engine, we identify the four strokes of the cycle as follows, see Fig. 1: The first optical pumping step realizes isochoric heating of the spin (heat transfer $Q^{(1)}$). For an ion positioned at $x > 0$, the effective restoring force is increased. In the second step, the harmonic oscillation half-cycle leads to a decrease of ω_z', i.e. isentropic expansion (consumption of work $W^{(2)}$ from the flywheel), as the ion moves to $x < 0$. Isochoric cooling takes place in the third step (heat transfer $Q^{(3)}$). This step again increases the effective restoring force. Then, the final oscillation half-cycle leads to an increase of ω_z', i.e. isentropic compression (release of work $W^{(4)}$ to the flywheel). As energy is continuously stored in the flywheel, the amplitude of the harmonic oscillation increases during the operation of the engine. Since the internal Zeeman energy of the spin scales with the oscillator displacement, the cycle is not closed, and the power increases with the number of cycles.

Quantifying work.—Due to its coupling with the baths, the spin's orientation is intrinsically uncertain, giving rise to a random spin-dependent force acting on the flywheel. This leads to fluctuations in the energy transferred to the flywheel during the isentropic strokes. Even for an ideal

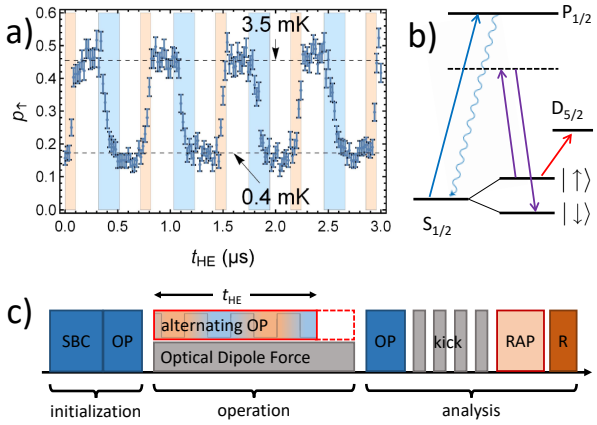


FIG. 2. **a)** Measured probabilities to find the spin in $|\uparrow\rangle$ throughout the engine operation. The colored areas indicate that the pump laser is switched on (pink: heating, blue: cooling). The equilibrium probabilities indicated by the horizontal dashed lines indicate the optical pumping operations, emulating the equilibration with reservoirs at temperatures T_C and T_H. **b)** Relevant atomic levels of $^{40}Ca^+$, showing the working-medium levels $|\downarrow\rangle$ and $|\uparrow\rangle$, the transition to the metastable $D_{5/2}$ level utilized for spin readout (red arrow), the stimulated Raman transition for probing (purple arrows) and the cycling transition utilized for optical pumping and readout (blue arrows). **c)** Experimental sequence for the reconstruction of the flywheel $\mathcal{Q}$ function (see text), indicating sideband cooling (SBC), optical pumping (OP), rapid adiabatic passage (RAP) and spin readout (R).

Otto cycle with fast, perfectly timed isochores and disregarding other experimental imperfections, the flywheel executes a random walk in phase space, whose statistical properties are determined by the equilibrium spin populations [28]. As a result, only a fraction of the deposited energy constitutes useful, extractable work, while the remainder increases the flywheelâ€™s entropy.

The flywheel's work content is quantified by its *ergotropy*, i.e. the maximum work that can be extracted via a cyclic unitary transformation [23]. It is defined as $\mathcal{W} = \mathrm{Tr}[\hat{H}_{\mathrm{HO}}\hat{\rho}] - \mathrm{Tr}[\hat{H}_{\mathrm{HO}}\hat{\rho}_p]$, where $\hat{\rho}$ is the state of the flywheel and $\hat{\rho}_p$ is the *passive state* unitarily related to $\hat{\rho}$ [28]. The ergotropy represents the amount of ordered energy stored in the flywheel while disregarding random contributions such as thermal fluctuations. Measuring the engine's work output thus requires us to characterize the state of the flywheel resulting from operation of the engine.

Experimental realization.—We store a single $^{40}Ca^+$ ion trapped in a miniaturized Paul trap [29], at a secular trap frequency of $\omega_t \approx 2\pi\times 1.4$ MHz along the x-axis. The Zeeman sublevels of the $S_{1/2}$ electronic ground state, i.e. the two-level system working agent of the engine, are denoted by $|\uparrow\rangle$ and $|\downarrow\rangle$ (Fig. 2 b). A constant magnetic field yields a Zeeman splitting between these of $\omega_z \approx 2\pi \times 13$ MHz. The alternating optical pumping is carried out via laser pulses driving the $S_{1/2} \leftrightarrow P_{1/2}$ cycling transition near

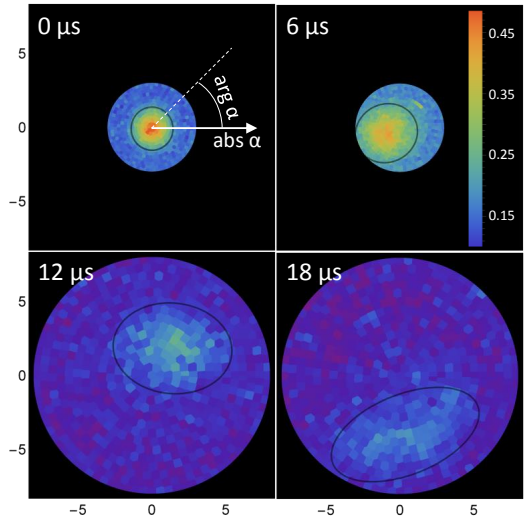


FIG. 3. Measured $\mathcal{Q}$ functions (raw data) for the flywheel at different times throughout the heat engine operation. Each pixel shows the result of 1000 independent experimental runs, and corresponds to a kick voltage determining $|\alpha|$ and a kick delay determining the phase $\arg\alpha$. The black lines are $1/e^2$ contours pertaining to fits of the $\mathcal{Q}$ function to the model Eq. (4). $|\alpha| = 1$ corresponds to an oscillation amplitude of 19 nm. For further evaluation, the raw data values are shifted and rescaled to account for imperfect population transfer and readout, such that the normalization $\int \mathcal{Q}(\alpha,\alpha^*)\mathrm{d}^2\alpha = 1$ is fulfilled, and that $\mathcal{Q}(\alpha,\alpha^*)$ assumes zero for large values of $|\alpha|$.

397 nm, at pulse durations shorter than half the trap period π/ω_t. For the hot (cold) isochore, the optical polarization is dynamically set to left (right) circular by means of an electro-optical modulator, which leads to population transfer $|\downarrow\rangle \rightarrow |\uparrow\rangle$ ($|\uparrow\rangle \rightarrow |\downarrow\rangle$). The intensities and pulse durations determine the spin polarizations at the end of the isochores and therefore the effective bath temperatures. We work with equilibrium spin polarizations of $\langle\hat{\sigma}_z\rangle^{(H)}$ = -0.084(4) and $\langle\hat{\sigma}_z\rangle^{(C)}$ =-0.656(6), which correspond to temperatures $T_H = 3.5(2)$ mK and $T_C = 0.40(1)$ mK according to Eq. (2). The SW - providing the coupling between spin and flywheel - is generated by two laser beams far-detuned from the cycling transition and controlled via acousto-optical modulators. This gives rise to a spin-dependent ac Stark shift, periodically varying along x at an amplitude of $\Delta_S = 2\pi \times 2.73(2)$ MHz $\ll \omega_z$.

The experimental sequence is depicted in Fig. 2 c). In each experimental run, the flywheel is initialized in its ground state via resolved sideband cooling [30], and the spin is initialized to a statistical mixture state corresponding to temperature T_C via optical pumping. Then, the SW is switched on we run the heat engine for a time t_{HE}, during which the alternating pumping is carried out.

After heat engine operation throughout t_{HE}, the SW is switched off. Then, the spin is pumped to $|\downarrow\rangle$ and its role is changed — rather than driving the engine, it is now employed as a probe for the final state of the flywheel $\hat{\rho}$. As the flywheel was initialized close to its ground state and energies in the few-quanta regime are to be resolved, a quantum-mechanical measurement scheme is ultimately required. We reconstruct the $\mathcal{Q}$ function of the flywheel

$$\mathcal{Q}(\alpha,\alpha^*) = \tfrac{1}{\pi}\langle 0|\,\hat{D}^\dagger(\alpha)\hat{\rho}\hat{D}(\alpha)\,|0\rangle\,. \tag{3}$$

This quantity is the probability to find the flywheel in the ground state after application of a displacement kick $\hat{D}(\alpha)$, and represents a quasi-probability distribution in phase space. The state reconstruction measurement starts with a displacement 'kick' operation of complex amplitude α on the flywheel. This operation is carried out by applying calibrated voltage pulses to neighboring trap segments [31]. After the kick, the population of all states $|n,\downarrow\rangle$ is transferred to $|n-1,\uparrow\rangle$. This is possible *only* for $n \neq 0$, therefore only the population pertaining to $n = 0$ remains in $|\downarrow\rangle$. This is realized via rapid adiabatic passage (RAP) on the first red sideband of the stimulated Raman transition between $|\uparrow\rangle$ and $|\downarrow\rangle$. Finally, spin readout via population transfer $|\uparrow\rangle \rightarrow \mathrm{D}_{5/2}$ to a metastable state [30] and subsequent detection of state-dependent fluorescence upon driving the cycling transition yields a 'bright' result at a probability corresponding to the $\mathcal{Q}$ function value Eq. (3). A similar method has been used e.g. in Refs. [14, 22].

The $\mathcal{Q}$ function is reconstructed in polar phase space coordinates by scanning $|\alpha|$ via the kick voltage amplitude and $\arg\alpha$ via the kick delay time with respect to the onset of the heat engine operation. For increasing values of $|\alpha|$, the resolution of $\arg\alpha$ is increased, such that the support of $\mathcal{Q}(\alpha,\alpha^*)$ in phase space is scanned at roughly constant steps.

Results.—We reconstruct $\mathcal{Q}(\alpha,\alpha^*)$ for different heat engine runtimes t_{HE}, in steps of $t_{\mathrm{HE}}^{(i)} = i\ \Delta t_{\mathrm{HE}}$ with $\Delta t_{\mathrm{HE}} = 3\,\mu$s, up to a duration of about 25 flywheel oscillation periods. Examples of reconstructed $\mathcal{Q}$ functions are shown in Fig. 3, revealing the nature of the final flywheel states. The quasi-probability peaks around a fixed amplitude and phase, indicating coherent oscillations. Furthermore, the support of the distribution increases asymmetrically beyond the uncertainty limit, indicating a thermal component induced by spin fluctuations and squeezing by the anharmonic SW potential. We therefore model the resulting flywheel states as displaced squeezed thermal states (DSTS):

$$\hat{\rho}_{\mathrm{DST}}(\beta,\zeta,\bar{n}) = \hat{D}(\beta)\hat{S}(\zeta)\hat{\rho}_{\mathrm{th}}(\bar{n})\hat{S}^\dagger(\zeta)\hat{D}^\dagger(\beta), \tag{4}$$

$$\hat{\rho}_{\mathrm{th}}(\bar{n}) = \sum_n \frac{\bar{n}^n}{(\bar{n}+1)^{n+1}}\,|n\rangle\langle n|\,, \tag{5}$$

with the thermal state $\hat{\rho}_{\mathrm{th}}(\bar{n})$ pertaining to the mean thermal phonon number $\bar{n}$, the squeezing operator $\hat{S}(\zeta)$ and the displacement operator $\hat{D}(\beta)$. The squeezing excitation is small as compared to thermal and displacement excitations. For obtaining estimates of the param-

eters $\bar{n}, \beta, \zeta$ for each reconstructed flywheel state, we fit the model Eq. (4) to given $\mathcal{Q}$ function data. To that end, for each test parameter set $\{\beta, \zeta, \bar{n}\}$, a density matrix is computed in a truncated number state basis from Eq. (4), from which the $\mathcal{Q}$ function values at the probed phase space coordinates are computed directly from Eq. (3). The fit minimizes the root-mean-square difference between the measured and model $\mathcal{Q}$ function values.

The DSTS model provides a description of the flywheel energetics. The ergotropy $\mathcal{W}$ and mean energy $E = \mathrm{Tr}[\hat{H}_{\mathrm{HO}}\hat{\rho}_{\mathrm{DST}}]$ are given respectively by [28]

$$\mathcal{W} = \hbar\omega_t|\beta|^2 + \hbar\omega_t \sinh^2(|\zeta|)(2\bar{n}+1), \tag{6}$$

$$E = \mathcal{W} + \hbar\omega_t\bar{n}. \tag{7}$$

The dominant contribution to the ergotropy derives from the oscillatory motion represented by β, with a further squeezing contribution. Conversely, thermal fluctuations increase the mean energy by an amount $\hbar\omega_t\bar{n}$, that cannot be extracted as work. Note, however, that squeezing catalyzes the extraction of work from thermal fluctuations [25] via the term proportional to $\sinh^2(|\zeta|)\bar{n}$ in Eq. (6).

The energy and ergotropy deposited in the flywheel are displayed in Fig. 4, together with the relative energy fluctuations $\Delta E/E$, where $\Delta E^2 = \mathrm{Tr}[\hat{H}_{\mathrm{HO}}^2\hat{\rho}_{\mathrm{DST}}] - E^2$. The experimental results show qualitative agreement with simulations of a Lindblad master equation describing the Otto cycle. Importantly, our theoretical model incorporates the full Hamiltonian (1), which is nonlinear in $\hat{x}$. The assumption that the ion remains close to the SW node, so that $k_{\mathrm{SW}}\langle\hat{x}\rangle \ll 1$, breaks down after about five engine cycles. As a consequence, the engine transitions from its initial onset behavior, with ergotropy increasing quadratically in time, to a later regime where the curvature of the SW potential limits the growth of ergotropy to be approximately linear. The squeezing contribution to the ergotropy amounts to 1.9(3) quanta at $t_{\mathrm{HE}} = 18\,\mu\mathrm{s}$.

Our measurements show that the flywheel's ergotropy $\mathcal{W}$ remains strictly less than its energy E due to the presence of thermal excitation. However, the *fraction* $\mathcal{W}/E$ grows over time, indicating an increasingly ordered deposition of energy in the flywheel. This is reflected in the behavior of $\Delta E/E$, which exhibits a crossover from an initial transient increase dominated by thermal fluctuations to asymptotic decay at longer times [28]. Note that even a pure coherent state, which would arise from unitary transfer of work to the flywheel, would still exhibit Poissonian energy fluctuations. As shown in Fig. 4(b), the measured energy fluctuations significantly exceed this "displacement limit". These results demonstrate that the extractable work produced by microscopic engines is reduced by intrinsic fluctuations. However, in order to distinguish useless thermal energy from useful deposited work, one must go beyond energy statistics to quantitatively describe the thermodynamic performance of such engines — for which ergotropy is the relevant quantity.

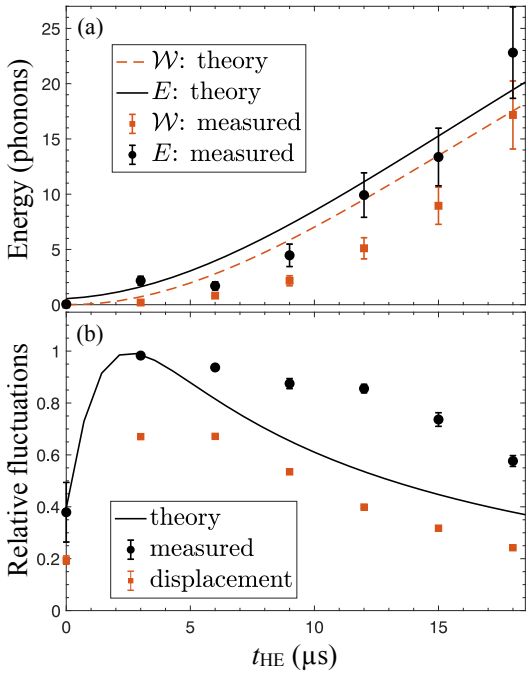


FIG. 4. Results: (a) measured energy E, ergotropy $\mathcal{W}$ and (b) relative energy fluctuations $\Delta E/E$, compared to (cycle-averaged) predictions of the master equation [28]. In (b) we also plot the relative fluctuations of a coherent state with the measured displacement β, i.e., $(\Delta E/E)_{\mathrm{displ}} = |\beta|/(|\beta|^2 + \frac{1}{2})$. In the simulations, the flywheel starts in a thermal state with the measured initial energy. Note that the relative fluctuation values exhibit small error bars as both statistical and systematic errors of ΔE and E are correlated.

The obtained ergotropy values fall significantly short from the simulation, while the relative energy fluctuations exceed the simulation values. This discrepancy between theory and experiment can be attributed to imperfections such as photon recoils during optical pumping, phase jitters of the SW and off-resonant scattering from the SW, which are not included in the simulation. See the Supplemental Material for details of the theoretical model and error analysis [28].

Conclusion & outlook.—We have experimentally demonstrated the operation of a single spin-$\frac{1}{2}$ heat engine coupled to a harmonic-oscillator flywheel, and we have characterized the finite-time thermodynamic performance of the combined engine-flywheel system. Furthermore, we have shown that $\mathcal{Q}$-function measurements together with a DSTS ansatz allow for an accurate assessment of the energetic capability of our microscopic engine via the ergotropy, i.e. the maximum amount of work which can be extracted from the flywheel by a cyclic unitary protocol. Our results reveal the importance of fluctuations in machines operating on single atomic degrees of freedom.

We stress that while our measurement method is intrinsically quantum mechanical, and while we initialize the flywheel in its ground state, the resulting states of

the flywheel are consistent with a semi-classical model. This is a consequence of the operational principle implemented here, which requires optical pumping, i.e.strong incoherent coupling of the spin engine to reservoirs to accomplish heat transfer.

Ultimately, one would seek to establish reservoirs consisting of sets of trapped ions rather than external control fields, which would open up a plethora of possibilities for studying thermal machines comprised of well-controlled microscopic quantum systems. Further extensions of the spin heat engine could encompass limit-cycle operation by adding persistent laser cooling of the flywheel, and demonstrating autonomous operation [32, 33]. We also note that irreversible entropy production can be inferred from $\mathcal{Q}$ functions via the Wehrl entropy [34] and that our platform may allow investigation of links between ergotropy and correlations [35]. Our experiment opens the door to further explorations of nano-scale thermodynamics where a work repository is explicitly included.

We acknowledge financial support by the JGU Mainz, helpful discussions with Martin Plenio, and early-stage contributions by Marcelo Luda and Johannes Rossnagel. JG is supported by a SFI-Royal Society University Research Fellowship. JG and MTM acknowledge funding from the European Research Council (ERC) under the European Union's Horizon 2020 research and innovation program (grant agreement No. 758403). FSK and UGP acknowledge funding from DeutscheForschungsgemeinschaft (FOR 2724).

* Present address: LIAF - Laboratorio de Iones y Atomos Frios, Departamento de Fisica & Instituto de Fisica de Buenos Aires, 1428 Buenos Aires, Argentina

† poschin@uni-mainz.de

[1] P. G. Steeneken, K. L. Phan, M. J. Goossens, G. E. J. Koops, G. J. A. M. Brom, C. van der Avoort, and J. T. M. van Beek, Nature Phys. **7**, 354â€“359 (2011).
[2] V. Blickle and C. Bechinger, Nature Phys. **8**, 143 (2012).
[3] I. A. Martinez, E. Roldan, L. Dinis, D. Petrov, J. M. R. Parrondo, and R. A. Rica, Nature Phys. **12**, 67 (2016).
[4] J. Roßnagel, S. T. Dawkins, K. N. Tolazzi, O. Abah, E. Lutz, F. Schmidt-Kaler, and K. Singer, Science **352**, 325 (2016).
[5] G. Maslennikov, S. Ding, R. Hablützel, J. Gan, A. Roulet, S. Nimmrichter, J. Dai, V. Scarani, and D. Matsukevich, Nat. Commun. **10** (2019), 10.1038/s41467-018-08090-0.
[6] J. Klatzow, J. N. Becker, P. M. Ledingham, C. Weinzetl, K. T. Kaczmarek, D. J. Saunders, J. Nunn, I. A. Walmsley, R. Uzdin, and E. Poem, Phys. Rev. Lett. **122**, 110601 (2019).
[7] J. V. Koski, V. F. Maisi, J. P. Pekola, and D. V. Averin, Proc. Natl. Acad. Sci. **111**, 13786 (2014).
[8] J. P. S. Peterson, T. B. Batalhao, M. Herrera, A. M. Souza, R. S. Sarthour, I. S. Oliveira, and R. M. Serra, arXiv:1803.06021.
[9] F. L. Curzon and B. Ahlborn, Am. J. Phys. **43**, 22 (1975).
[10] R. Alicki, J. Phys. A: Math. Gen. **12**, L103 (1979).
[11] P. Talkner and P. Hänggi, Phys. Rev. E **93**, 022131 (2016).
[12] C. Jarzynski, Phys. Rev. Lett. **78**, 2690 (1997).
[13] U. Seifert, Rep. Prog. Phys. **75**, 126001 (2012).
[14] S. An, J. Zhang, M. Um, D. Lv, Y. Lu, J. Zhang, Z. Yin, H. T. Quan, and K. Kim, Nature Phys. **11**, 193 (2015).
[15] R. Kosloff, J. Chem. Phys. **80**, 1625 (1984).
[16] M. O. Scully, Phys. Rev. Lett. **88**, 050602 (2002).
[17] N. Brunner, M. Huber, N. Linden, S. Popescu, R. Silva, and P. Skrzypczyk, Phys. Rev. E **89**, 032115 (2014).
[18] A. del Campo, J. Goold, and M. Paternostro, Scientific Reports **4**, 6208 (2014).
[19] M. Campisi and R. Fazio, Nature Communications **7**, 11895 EP (2016), article.
[20] G. Watanabe, B. P. Venkatesh, P. Talkner, and A. del Campo, Phys. Rev. Lett. **118**, 050601 (2017).
[21] A. Levy, L. Diosi, and R. Kosloff, Phys. Rev. A **93**, 052119 (2016).
[22] D. Lv, S. An, M. Um, J. Zhang, J.-N. Zhang, M. S. Kim, and K. Kim, Phys. Rev. A **95**, 043813 (2017).
[23] A. Allahverdyan, R. Balian, and T. M. Nieuwenhuizen, EPL **67**, 565 (2004).
[24] D. Gelbwaser-Klimovsky, R. Alicki, and G. Kurizki, EPL **103**, 60005 (2013).
[25] A. Ghosh, C. L. Latune, L. Davidovich, and G. Kurizki, Proc. Natl. Acad. Sci. **114**, 12156 (2017).
[26] U. Poschinger, A. Walther, K. Singer, and F. Schmidt-Kaler, Phys. Rev. Lett. **105**, 263602 (2010).
[27] C. T. Schmiegelow, H. Kaufmann, T. Ruster, J. Schulz, V. Kaushal, M. Hettrich, F. Schmidt-Kaler, and U. G. Poschinger, Phys. Rev. Lett. **116**, 033002 (2016).
[28] See Supplemental Material at [URL will be inserted by publisher] for a detailed error discussion.
[29] S. Schulz, U. Poschinger, F. Ziesel, and F. Schmidt-Kaler, New J. Phys. **10**, 045007 (2008).
[30] U. Poschinger, G. Huber, F. Ziesel, M. Deiss, M. Hettrich, S. Schulz, G. Poulsen, M. Drewsen, R. Hendricks, K. Singer, and F. Schmidt-Kaler, J. Phys. B: At. Mol. Opt. Phys. **42**, 154013 (2009).
[31] F. Ziesel, T. Ruster, A. Walther, H. Kaufmann, S. Dawkins, K. Singer, F. Schmidt-Kaler, and U. Poschinger, J. Phys. B: At. Mol. Opt. Phys. **46**, 104008 (2013).
[32] F. Tonner and G. Mahler, Phys. Rev. E **72**, 066118 (2005).
[33] D. Gelbwaser-Klimovsky and G. Kurizki, Phys. Rev. E **90**, 022102 (2014).
[34] J. P. Santos, L. C. Céleri, F. Brito, G. T. Landi, and M. Paternostro, Phys. Rev. A **97**, 052123 (2018).
[35] G. Francica, J. Goold, F. Plastina, and M. Paternostro, npj Quantum Information **3**, 12 (2017).

A spin heat engine coupled to a harmonic oscillator flywheel: Supplemental material

D. von Lindenfels,[1] O. Gräb,[1] C. T. Schmiegelow,[1,*] V. Kaushal,[1] J. Schulz,[1]
Mark T. Mitchison,[2] John Goold,[2] F. Schmidt-Kaler,[1] and U. G. Poschinger[1,†]

[1] *QUANTUM, Institut für Physik, Universität Mainz, Staudingerweg 7, 55128 Mainz, Germany*
[2] *School of Physics, Trinity College Dublin, College Green, Dublin 2, Ireland*

I. EXPERIMENTAL METHODS

A. Optical pumping

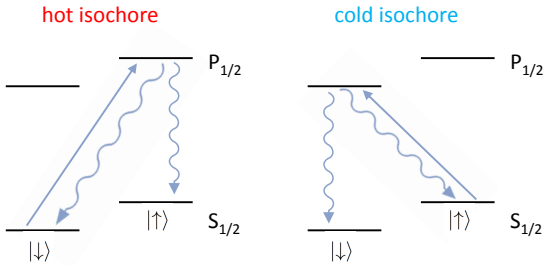


FIG. 1. Optical pumping. It is shown how the pumping laser beam at alternating circular polarization transfers population between the spin levels throughout the hat and cold isochores, within the $S_{1/2}$ and via the $P_{1/2}$ state manifolds.

For the alternating optical pumping, we employ a laser beam driving the $S_{1/2} \leftrightarrow P_{1/2}$ cycling transition near 397 nm, as shown in Fig. 1. The beam is propagating in parallel to the external magnetic field, such that it drives $\Delta m = \pm 1$ transitions. Its polarization is dynamically controlled using an electro-optical modulator (EOM), which dynamically switches between σ_+ and σ_- circular polarization. The pump pulse durations are shorter than a half trap cycle π/ω_t. It would take on average three scattering events to flip the spin. The pump pulse intensities are chosen such that much less than three photons per pump pulse are scattered, i.e. the mean change of spin polarization per pump pulse is $|\delta\langle\hat{\sigma}_z\rangle| \ll 2$. The spin polarization after the heating (cooling) pump pulses determine the hot(cold) temperatures according to Eq. 2 from the manuscript.

We achieve pumping rates of up to $3 \times 10^6\,\mathrm{s}^{-1}$, which allows for efficient optical pumping on timescales shorter than a trap period. The beam is additionally switched on and off via an acousto-optical modulator (AOM). While the duration of the pumping pulses for heating is fixed to 100 ns, the duration of the cooling pulse is calibrated in order to minimize coherent excitation of the flywheel induced by the resonant radiation pressure force, see Sec. II D. To that end, measurements are performed where the heat engine is operated with the SW switched off, such that flywheel excitation is only caused by photon scattering recoil and resonant radiation pressure. An electrical kick (see Sec. I C) is applied after heat engine operation, and then the flywheel state is probed on different sidebands of the stimulated Raman transition $|\downarrow\rangle \leftrightarrow |\uparrow\rangle$ in order to obtain a measure which grows monotonously with the flywheel excitation [1]. The contrast at which this excitation varies w.r.t a delay time between the heat engine start and the kick pulse is proportional to the radiation-pressure induced coherent excitation of the flywheel. The cooling pump pulse duration of 200 ns is found to minimize this value, i.e. the total recoil momenta from heating and cooling pulses roughly balance for each cycle.

B. Spin-dependent forces

The optical dipole force is generated by two laser beams in lin $\perp$ lin configuration, both directed at 45° to the trap axis and at 90° to each other, such that the difference wavevector is aligned along the trap x-axis [2]. The beams are detuned by about $2\pi \times 150$ GHz from the $S_{1/2} \leftrightarrow P_{1/2}$ 'cycling' transition near 397 nm. Both beams have the same optical frequency, which gives rise to a static SW beat pattern along x-axis, at a differential ac-Stark shift amplitude of $\Delta_S = 2\pi \times 2.73(2)$ MHz and an effective wavenumber (modulus of the difference wavevector) of about $2\pi/280$ nm.

C. Electrical kicks

$\mathcal{Q}$ functions are reconstructed by electrical kicks, generating a displacement operation $\hat{D}(\alpha)$. This operation is realized by train of 10 voltage pulses, spaced by the trap period and applied to the trap segments neighboring the trap site. The modulus of the displacement $|\alpha|$ is controlled by the voltage amplitude V_k of the pulses [3]. The maximum voltage amplitude of 0.7 V gives rise to an electric field of 320 V/m at the ion location. The pulse train at maximum amplitude yields a displacement modulus of $|\alpha| \approx 8$. The phase of α is controlled by the delay of the first kick with respect to the onset of heat engine operation.

* Present address: LIAF - Laboratorio de Iones y Atomos Frios, Departamento de Fisica & Instituto de Fisica de Buenos Aires, 1428 Buenos Aires, Argentina
† poschin@uni-mainz.de

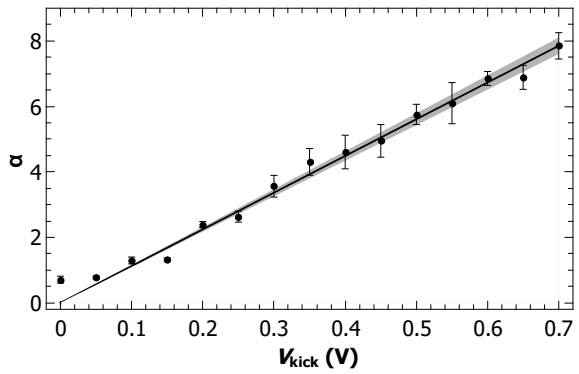


FIG. 2. Calibration of the electrical kicks. The estimated displacement modulus α is shown versus the voltage amplitude of a resonant train of 10 electrical kick pulses, V_{kick}, along with a linear fit and its uncertainty band.

The relation between $|\alpha|$ and V_k is calibrated by a set of separate measurements. Here, we carry out sequences where a train of 10 electrical kicks of amplitude V_k is followed by a probe pulse of variable duration on the stimulated Raman transition. The carrier transition $|\uparrow\rangle \leftrightarrow |\downarrow\rangle$ is probed along with its first and second motional sidebands. The measured populations $P_{|\uparrow\rangle}$ versus the probe pulse durations are fitted to a Rabi flopping model [1], based on the assumption that the axial mode is in a coherent state. For the maximum kick voltage amplitude, coherent displacements corresponding to a mean phonon number of about 60 phonons are obtained. The dependence of $|\alpha|$ on V_k is linear, and a fit yields the relation

$$|\alpha| = c\, V_k, \tag{1}$$

with the best fit parameter $\bar{c} = 10.60\ V^{-1}$ and the uncertainty $\sigma_c = 0.49\ V^{-1}$. The results of the calibration measurement are shown in Fig. 2.

D. Ground state discrimination

For detecting the population in the flywheel state $|n = 0\rangle$, we carry out rapid adiabatic passage (RAP) on the first red motional sideband of the stimulated Raman transition, i.e. $|\uparrow, n\rangle \leftrightarrow |\downarrow, n-1\rangle$. This ensures near-perfect population transfer despite the dependence of the red sideband Rabi frequency on the motional quantum number n. We employ laser pulses with sine-square intensity profile, a total duration of 100 µs, a frequency chirp rate of $2\,\mathrm{kHz\,\mu s^{-1}}$, and a peak Rabi frequency on the transition $|\downarrow, 1\rangle \leftrightarrow |\uparrow, 0\rangle$ of $\eta\Omega_{\max} = 2\pi \times 22\,\mathrm{kHz}$. This leads to population transfer with > 90 % fidelity for a wide range of motional quantum numbers $0 < n \lesssim 60$.

E. Spin readout

For spin readout, we selectively transfer population from $|\downarrow\rangle$ to the metastable $D_{5/2}$ state via RAP on the $S_{1/2} \leftrightarrow D_{5/2}$ quadrupole transition, driven by laser pulses near 729 nm, followed by detection of state-dependent fluorescence upon driving the cycling transition [4].

II. $\mathcal{Q}$ FUNCTION MEASUREMENT: ERROR ANALYSIS

The reconstruction scheme for the $\mathcal{Q}$ functions and therefore the quantities derived from these data are subject to statistical and systematic errors. We have identified and accounted for the following error sources:

A. Statistical errors

Statistical error result from the binomial statistical errors of the spin readout underlying $\mathcal{Q}$ function measurement. Each point in phase space is probed $N = 1000$ times, resulting in errors between 0.005 and 0.015 for each data point. The propagation of the statistical errors on the values for energy and ergotropy is quantitatively analyzed by means on nonparametric bootstrapping: For each measured raw data $\mathcal{Q}_i^{(meas)}(\alpha, \alpha^*)$, 50 sets of artificial data is generated according to a binomial distribution for each probed point in phase space: $\mathcal{Q}_i^{(BS)}(\alpha, \alpha^*) \sim \mathrm{binomial}\left(N, \mathcal{Q}_i^{(meas)}(\alpha, \alpha^*)\right)$. Each artificial data set is evaluated via the same fitting procedure as for the measurement data. This yields a statistical sample of energy and ergotropy values, from which confidence intervals can be computed. We performed *parametric* bootstrapping, where for each measurement dataset, a density matrix is generated from the fit parameters, from which in turn 50 sets of artificial data is generated and fitted. Both methods yield statistically consistent mean fit parameters and confidence intervals.

B. Displacement calibration

The measurement for calibrating the $\mathcal{Q}$ function argument $|\alpha|$ in terms of the kick voltage V_k discussed in Sec. I C has a finite accuracy. The relative uncertainty of 4.6 % of the conversion factor c in Eq. 1 translates into an uncertainty of the radial scaling of the $\mathcal{Q}$ functions. We define the radial scaling deviation

$$\xi = \frac{c}{\bar{c}} - 1. \tag{2}$$

The mean energy depending on ξ is given by

$$E_\xi = \int d\phi \int d|\alpha|(1+\xi)|\alpha| \left((1+\xi)^2|\alpha|^2 - \tfrac{1}{2}\right) \mathcal{Q}(\alpha) \tag{3}$$

$$\approx E + \xi\left(3E + \tfrac{1}{2}\right) \tag{4}$$

Therefore

$$\frac{dE_\xi}{d\xi}|_{\xi=0} = 3E + \tfrac{1}{2} \tag{5}$$

and

$$\sigma_E^{(cal)} = \frac{3E + \frac{1}{2}}{\bar{c}}\sigma_c \tag{6}$$

C. Secular frequency drift

The axial secular frequency ω_t of the flywheel is subject to measurement uncertainty and drift. Resolved sideband spectroscopy on the stimulated Raman transition yields measurement accuracy of about $\delta_t \approx 2\pi \times 1\,\mathrm{kHz}$. The measurement scheme is affected in different ways by static offsets / slow drifts and by shot-to-shot fluctuations of ω_t.

In the first case, a mismatch between ω_t and the switching rate of the optical pumping pulses leads to a suboptimal performance of the heat-engine / flywheel system, as the effective driving force acting on the flywheel becomes out-of-phase during the operation. At the maximum operation time, the phase mismatch would be $\delta_t \times 20\,\mu\mathrm{s} \approx 0.13\mathrm{rad}$, which would lead to an insignificant performance reduction of about 0.2% in terms of deposited energy. A similar error mechanism occurs throughout the final displacement operation via a train of 10 electrical kicks as described in Sec. I C, which can also be seen as resonant excitation of the flywheel. As the duration of the kick operation is similar to the maximum engine operation time, this also leads to worst-case systematic errors in terms of mean energy of below 1%.

Fast fluctuations of ω_t on timescales below the acquisition time of one set of $\mathcal{Q}$ function data would lead to additional dephasing. Ramsey-type measurements of the motional coherence on number state superpositions $|0\rangle + |1\rangle$ yield coherence times of several tens of milliseconds, and the overall drift is less than $2\pi \times 1\,\mathrm{kHz}$ between different measurement runs. Therefore, we can exclude fast fluctuations and drifts of ω_t as a significant source of statistical or systematic errors.

D. Radiation pressure background

Background excitation was measured for several values of operation times t_{HE} via a full reconstruction of the $\mathcal{Q}$ function after operation throughout t_{HE} with the alternating optical pumping active but the SW switched off. The results are shown in Fig. 3. By 18 µs, a mean energy of 2.1(3) phonons and an ergotropy of 0.67(7) phonons is reached, resulting from random photon recoils throughout the optical pumping and residual resonant radiation pressure force resulting the fact that the overall number of scattered photons is not exactly balanced for the two different pumping strokes. The minimization of the net radiation pressure force is described in Sec. I A.

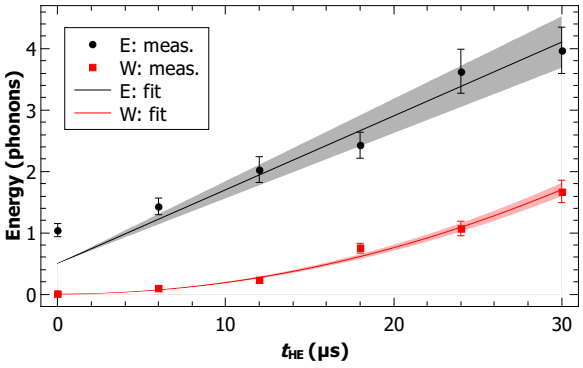


FIG. 3. Background excitation measurement. Energy and ergotropy are inferred from $\mathcal{Q}$ function measurements, where the engine is run without the SW switched on, i.e. only the optical pumping is carried out. The linear increase of the energy is consistent with the expected heating due to photon recoils, whereas the quadratic increase of the ergotropy is due to residual uncompensated resonant radiation pressure. Note that the maximum operation time of the heat engine is 18 µs.

For the background measurement, the ergotropy increase exhibits a quadratic behavior, which confirms that this is caused by a resonant radiation pressure force. This is a parasitic effect, caused by imperfecly calibrated operation parameters, add spuriously adds to the actual work generated by the heat engine. Therefore, the ergotropy data shown Fig. 4a) in the main manuscript has been corrected for this effect, i.e. the background excitation has been subtracted.

III. THEORETICAL METHODS

A. The concept of ergotropy

Ergotropy has emerged as an important concept in the field of quantum thermodynamics. It is defined as the *maximum* amount of work that can be extracted from a quantum state by means of a cyclical unitary transformation [5]. Explicitly, consider a quantum system described by a generic Hamiltonian

$$\hat{H} = \sum_k \epsilon_k |\epsilon_k\rangle \langle\epsilon_k| ,$$

where the eigenvalues are ordered so that $\epsilon_k \leq \epsilon_{k+1}$. The initial density matrix can always be expressed in the diagonal form

$$\hat{\rho} = \sum_k r_k |r_k\rangle \langle r_k| .$$

The state $\hat{\rho}$ is *passive* with respect to the Hamiltonian $\hat{H}$ [6, 7] if $[\hat{\rho}, \hat{H}] = 0$ and $r_n \geq r_m$ whenever $\epsilon_n < \epsilon_m$. Thermal states in particular are always passive, since they are energy-diagonal and satisfy $r_n/r_m = \mathrm{e}^{\beta(\epsilon_m - \epsilon_n)}$, with

$\beta = 1/k_B T$ the inverse temperature.

States that are not passive — such as the dynamical state of the flywheel in this experiment — can deliver output work. In order to extract the useful energy from a non-passive state we assume that we are able to control the Hamiltonian in some time interval $[0, \tau]$ in such a way that

$$\hat{H}(0) = \hat{H}(\tau) = \hat{H}.$$

The time evolution from $t = 0$ to $t = \tau$ is given by the unitary operator $\hat{U} = \mathrm{T}\exp[\int_0^\tau \mathrm{d}t\, \hat{H}(t)/\mathrm{i}\hbar]$. This is an isentropic evolution and therefore the energy change of the system is equal to the extracted work

$$W_{\mathrm{ex}} = \mathrm{Tr}\left\{\hat{H}\left(\hat{\rho} - \hat{U}\hat{\rho}\hat{U}^\dagger\right)\right\}.$$

The maximum quantity of work that can be extracted is called ergotropy [5] and customarily denoted $\mathcal{W}$. It is obtained by choosing $\hat{U}$ to maximise W, i.e., $\mathcal{W} = \max_{\hat{U}} W_{\mathrm{ex}}$. The final state that results from this maximal work extraction protocol is the unique passive state $\hat{\rho}_p$ pertaining to the initial state $\hat{\rho}$. This passive state has the form

$$\hat{\rho}_p = \sum_k r_k \left|\epsilon_k\right\rangle \left\langle\epsilon_k\right|,$$

where $\{r_k\}$ are the eigenvalues of the initial state $\hat{\rho}$ ordered such that $r_k \geq r_{k+1}$. Therefore, the ergotropy is given explicitly by

$$\begin{aligned}\mathcal{W} &= \mathrm{Tr}\left\{\hat{H}\hat{\rho}\right\} - \mathrm{Tr}\left\{\hat{H}\hat{\rho}_p\right\} \\ &= \sum_{j,k} r_k \epsilon_j (|\langle\epsilon_j|r_k\rangle|^2 - \delta_{jk}).\end{aligned}$$

In the context of the flywheel, the ergotropy provides a useful operational quantity which allows to isolate the extractable component from the total energy change [8]. As one can see from the above formulae, non-passivity and hence the ability to extract work is attributed to both coherences and population inversions (in the energy eigenbasis). In addition, ergotropy has been linked to quantum correlations in an extended setup [9].

B. Energetics of displaced squeezed thermal states

A displaced, squeezed thermal state (DSTS) $\rho_{\mathrm{DST}}(\beta, \zeta, \bar{n})$ is defined by

$$\hat{\rho}_{\mathrm{DST}}(\beta, \zeta, \bar{n}) = \hat{D}(\beta)\hat{S}(\zeta)\hat{\rho}_{\mathrm{th}}(\bar{n})\hat{S}^\dagger(\zeta)\hat{D}^\dagger(\beta), \quad (7)$$

$$\hat{\rho}_{\mathrm{th}}(\bar{n}) = \sum_n \frac{\bar{n}^n}{(\bar{n}+1)^{n+1}} \left|n\right\rangle \left\langle n\right|, \quad (8)$$

$$\hat{S}(\zeta) = \exp\left(\frac{1}{2}\left[\zeta(\hat{a}^\dagger)^2 - \zeta^*\hat{a}^2\right]\right), \quad (9)$$

$$\hat{D}(\beta) = \exp\left(\beta\hat{a}^\dagger - \beta^*\hat{a}\right), \quad (10)$$

with thermal occupation $\bar{n}$, squeezing parameter $\zeta = r\mathrm{e}^{\mathrm{i}\phi}$ and displacement β. From this we may deduce the following expectation values

$$\langle\hat{a}\rangle = \beta, \quad (11)$$

$$\left\langle\hat{n} + \tfrac{1}{2}\right\rangle = \tfrac{1}{2}\cosh(2r)\,(2\bar{n}+1) + |\beta|^2, \quad (12)$$

$$\begin{aligned}\langle\hat{n}^2\rangle - \langle\hat{n}\rangle^2 &= \cosh(4r)\bar{n}(\bar{n}+1) \\ &\quad + \tfrac{1}{2}\sinh^2(2r) + |\beta\cosh(r) + \beta^*\mathrm{e}^{\mathrm{i}\phi}\sinh(r)|^2 \\ &\quad + 2\bar{n}|\beta\cosh(r) + \beta^*\mathrm{e}^{\mathrm{i}\phi}\sinh(r)|^2. \quad (13)\end{aligned}$$

Here we have explicitly separated Eq. (13) into three distinct contributions. The first line describes thermal fluctuations, the second line arises from coherences in the energy eigenbasis associated with displacement and squeezing, while the third line is a thermal-coherent cross term.

The passive state associated to $\hat{\rho}_{\mathrm{DST}}(\beta, \zeta, \bar{n})$ is the thermal state $\hat{\rho}_{\mathrm{th}}(\bar{n})$, since the two are unitarily related by Eq. (7) and all thermal states are passive by definition. The energy of the thermal state is $\mathrm{Tr}[\hat{H}_{\mathrm{HO}}\hat{\rho}_{\mathrm{th}}(\bar{n})] = \hbar\omega_t(\bar{n} + \frac{1}{2})$. Thus, the ergotropy of the DSTS is given by $\mathcal{W} = \hbar\omega_t(\langle\hat{n}\rangle - \bar{n})$. Together with Eq. (12) above, this implies Eqs. (6) and (7) in the main text.

C. Random-walk model

In this section we show how the dynamics of the flywheel may be understood as a random walk in phase space. We consider an idealised model of the Otto cycle with no motional heating due to spontaneous emission or other sources (e.g. micromotion, trap potential fluctuations etc.) and perfect timing of the engine strokes. We also make the simplifying assumption that the isochores occur instantaneously. As shown in the following section, this is a good approximation to a more realistic description that takes the finite isochore duration into account.

The free evolution of the spin-flywheel system is governed by the Hamiltonian $\hat{H}$ given in Eq. (1) of the main text. This Hamiltonan is block diagonal in the spin variables and thus may be written in the form

$$\hat{H} = \hat{\Pi}_\downarrow \otimes \hat{H}_\downarrow + \hat{\Pi}_\uparrow \otimes \hat{H}_\uparrow, \quad (14)$$

where $\hat{\Pi}_s = |s\rangle\langle s|$ is a projector onto an eigenstate of $\hat{\sigma}_z$ with spin projection $s = \downarrow, \uparrow$, and the spin-dependent flywheel Hamiltonian is

$$\hat{H}_{\uparrow,\downarrow} = \hbar\omega_t\left(\hat{a}^\dagger\hat{a} + \tfrac{1}{2}\right) \pm \frac{\hbar\Delta_S}{2}\sin(k_{\mathrm{SW}}\hat{x}), \quad (15)$$

with the plus (minus) sign corresponding to $\uparrow$ ($\downarrow$). Between isochores, the dynamics of the system is given by the unitary evolution operator over a half-period π/ω_t, which may be written as

$$\hat{U} = \hat{\Pi}_\downarrow \otimes \hat{U}_\downarrow + \hat{\Pi}_\uparrow \otimes \hat{U}_\uparrow, \quad (16)$$

where $\hat{U}_s = \mathrm{e}^{-\mathrm{i}\pi\hat{H}_s/\hbar\omega_t}$. The instantaneous isochores correspond to the map $\hat{\Pi}_s \to p_\downarrow^{c,h}\hat{\Pi}_\downarrow + p_\uparrow^{c,h}\hat{\Pi}_\uparrow$, which extends

to the spin-flywheel Hilbert space as

$$\mathcal{E}_{c,h}\hat{\rho} = \left(p_{\downarrow}^{c,h}\hat{\Pi}_{\downarrow} + p_{\uparrow}^{c,h}\hat{\Pi}_{\uparrow}\right) \otimes \mathrm{Tr}_S[\hat{\rho}], \tag{17}$$

where Tr_S denotes a partial trace over the spin. This map resets the spin to the appropriate thermal state while leaving the flywheel unaffected.

Starting directly after the hot isochore, each cycle consists of the composite map

$$\hat{\rho} \to \mathcal{E}_h \mathcal{U} \mathcal{E}_c \mathcal{U} \hat{\rho}, \tag{18}$$

where $\mathcal{U}\hat{\rho} = \hat{U}\hat{\rho}\hat{U}^\dagger$. Tracing over the spin yields a recursion relation for the flywheel state $\hat{\rho}_F^{(N)}$ after N cycles:

$$\begin{aligned}\hat{\rho}_F^{(N)} = {} & p_{\downarrow}^c p_{\downarrow}^h \hat{U}_{\downarrow\downarrow}\hat{\rho}_F^{(N-1)}\hat{U}_{\downarrow\downarrow}^\dagger + p_{\uparrow}^c p_{\uparrow}^h \hat{U}_{\uparrow\uparrow}\hat{\rho}_F^{(N-1)}\hat{U}_{\uparrow\uparrow}^\dagger \\ & + p_{\downarrow}^c p_{\uparrow}^h \hat{U}_{\downarrow\uparrow}\hat{\rho}_F^{(N-1)}\hat{U}_{\downarrow\uparrow}^\dagger + p_{\uparrow}^c p_{\downarrow}^h \hat{U}_{\uparrow\downarrow}\hat{\rho}_F^{(N-1)}\hat{U}_{\uparrow\downarrow}^\dagger,\end{aligned} \tag{19}$$

where $\hat{U}_{\downarrow\downarrow} = \hat{U}_{\downarrow}\hat{U}_{\downarrow}$, $\hat{U}_{\downarrow\uparrow} = \hat{U}_{\downarrow}\hat{U}_{\uparrow}$, etc. This describes a discrete-time random walk, which can be efficiently simulated by the following simple procedure: After each cycle, one of the four unitaries $\{\hat{U}_{\downarrow\downarrow}, \hat{U}_{\downarrow\uparrow}, \hat{U}_{\uparrow\downarrow}, \hat{U}_{\uparrow\uparrow}\}$ is applied at random according to the probability distribution $\{p_{\downarrow}^c p_{\downarrow}^h, p_{\downarrow}^c p_{\uparrow}^h, p_{\uparrow}^c p_{\downarrow}^h, p_{\uparrow}^c p_{\uparrow}^h\}$. Any observable can then be estimated by averaging over many such trajectories.

A further simplification is obtained by assuming small displacements from the SW node, i.e., $k_{\mathrm{SW}}\langle\hat{x}\rangle \ll 1$, which is a valid approximation for short engine operation times. Expanding the Hamiltonian to first order gives

$$\hat{H}_{\downarrow,\uparrow} = \hbar\omega_t(\hat{a}^\dagger\hat{a} + \tfrac{1}{2}) \pm \frac{\hbar\omega_t d}{2}\left(\hat{a} + \hat{a}^\dagger\right), \tag{20}$$

with the dimensionless displacement

$$d = \frac{\Delta_S k_{\mathrm{SW}} x_0}{\omega_t} \approx 0.416, \tag{21}$$

where $x_0 = \sqrt{\hbar/2m\omega_t}$ is the natural oscillator length. Eq. (20) is diagonalized by a displacement transformation $\hat{D}(\pm d/2)\hat{H}_{\uparrow,\downarrow}\hat{D}^\dagger(\pm d/2) = \hat{H}_{\mathrm{HO}}$. It follows immediately that

$$\hat{U}_{\uparrow} = \hat{P}\hat{D}(d), \quad \hat{U}_{\downarrow} = \hat{P}\hat{D}(-d), \tag{22}$$

where $\hat{P} = \mathrm{e}^{\mathrm{i}\pi\hat{a}^\dagger\hat{a}}$ is the parity (spatial inversion) operator.

Plugging Eq. (22) into Eq. (19) gives a simpler recursion relation

$$\begin{aligned}\hat{\rho}_F^{(N)} = {} & p_0\hat{\rho}_F^{(N-1)} + p_+\hat{D}(2d)\hat{\rho}_F^{(N-1)}\hat{D}^\dagger(2d) \\ & + p_-\hat{D}(-2d)\hat{\rho}_F^{(N-1)}\hat{D}^\dagger(-2d).\end{aligned} \tag{23}$$

This describes a one-dimensional discrete-time random walk along the $\hat{x}$ quadrature in phase space. The walker takes a step of size $\Delta x = 0, \pm 2d$ on each cycle. The corresponding probabilities are $p_+ = p_{\downarrow}^c p_{\uparrow}^h$, $p_- = p_{\uparrow}^c p_{\downarrow}^h$ and $p_0 = 1 - p_+ - p_-$. Note that the ratio of forward and backward probabilities is $p_+/p_- = \mathrm{e}^{(\beta_c - \beta_h)\omega_z}$, where $\beta_{c,h} = 1/k_B T_{c,h}$ (here we neglect the dependence of the effective spin precession frequency on $\langle\hat{x}\rangle$). Since we must have $\beta_c > \beta_h$ for engine operation, a forward step is more likely than a backward one. Moreover, even in the limit $T_c \to 0$ where $p_- \to 0$, we have $p_0 \neq 0$ (assuming that T_h is positive) so that the walker dynamics is always stochastic.

Assuming that the initial state of the flywheel $\hat{\rho}_F^{(0)}$ is the vacuum, the state after N steps is a statistical mixture of coherent states $|\alpha_N\rangle\langle\alpha_N|$ with (real) displacement $\alpha_N = \sum_{n=1}^N \Delta x_n$, where Δx_n are independent, identically distributed random variables taking the values $\Delta x_n = 0, \pm 2d$ with probability $p_0, p_\pm$. Normal-ordered quantum expectation values may thus be found from the moments of α_N using the formula $\langle(\hat{a}^\dagger)^q\hat{a}^p\rangle = \mathbb{E}[\alpha_N^{q+p}]$, where $\mathbb{E}[\cdot]$ denotes the average over random-walk trajectories. In turn, the moments of α_N can be obtained from derivatives of the generating function $G_N(s) = \mathbb{E}[\mathrm{e}^{s\alpha_N}] = [G_1(s)]^N$, where the single-step generating function is found to be

$$G_1(s) = 1 + 2\sinh(ds)(p_+\mathrm{e}^{ds} - p_-\mathrm{e}^{-ds}). \tag{24}$$

In particular, the mean displacement and the mean phonon number after N cycles are given by

$$\langle\hat{a}\rangle = 2d(p_+ - p_-)N, \tag{25}$$

$$\langle\hat{n}\rangle = 4d^2\left[p_+ + p_- - (p_+ - p_-)^2\right]N + \langle\hat{a}\rangle^2. \tag{26}$$

The mean displacement is linear in the number of steps. The phonon number has a linear component associated with the thermal spin fluctuations and a quadratic component due to the coherent displacement that dominates for large N. Higher moments can also be computed analytically from Eq. (24) although the resulting expressions are rather tedious. Here we simply note that the dominant contribution to the phonon number fluctuations for large N behaves as $\Delta n^2 = \langle\hat{n}^2\rangle - \langle\hat{n}\rangle^2 \sim N^3$, and thus the relative fluctuations decay asymptotically as $\Delta n/\langle\hat{n} + \frac{1}{2}\rangle \sim N^{-1/2}$, as expected for a diffusive process.

In order to connect these results with the model (7), we approximate the state after each step by a DSTS. For simplicity, we set $\zeta = 0$, since in the linear regime $k_{\mathrm{SW}}\langle\hat{x}\rangle \ll 1$ the squeezing excitation should be negligibly small. Comparing Eqs. (25) and (26) with the corresponding Eqs. (11) and (12), we deduce the change of β and $\bar{n}$ after one cycle:

$$\delta\beta = 2d(p_+ - p_-), \tag{27}$$

$$\delta\bar{n} = 4d^2\left[p_+ + p_- - (p_+ - p_-)^2\right]. \tag{28}$$

In other words, both the coherent displacement β and the thermal occupation $\bar{n}$ change linearly with the number of cycles.

This gives a simple understanding of the behaviour of the relative energy fluctuations via Eq. (13). At short times, where $E \lesssim \hbar\omega_t$, thermal noise dominates (i.e., the first term in Eq. (13)) and the relative fluctuations increase as $\Delta E/E \sim \sqrt{\bar{n}}$. After many cycles, the thermal-coherent cross term (i.e., the third line in Eq.(13)) is the dominant contribution to the fluctuations, while the energy grows as $E \sim \hbar\omega_t|\beta|^2$. We therefore find the asymptotic behaviour $\Delta E/E \sim \sqrt{\bar{n}}/|\beta| \sim N^{-1/2}$, in agreement with the exact random-walk solution.

We emphasise that these analytical results require that $k_{\mathrm{SW}}\langle\hat{x}\rangle \ll 1$, whereas Eq. (25) predicts that $k_{\mathrm{SW}}\langle\hat{x}\rangle \gtrsim 1$ after only $N = 10$ steps with the given experimental pa-

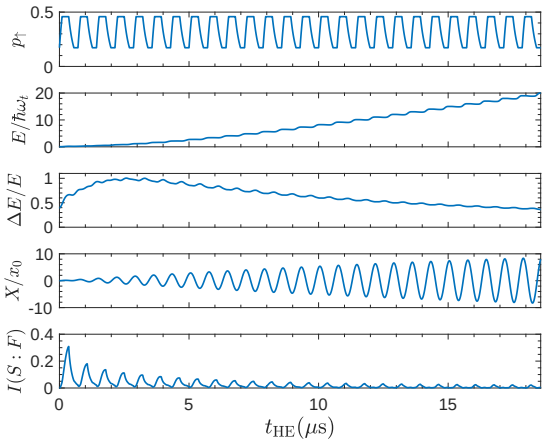


FIG. 4. Simulation of the master equation (29), taking parameters from the experiment. From top to bottom, the plots show the population of the spin's excited state $p_\uparrow$, the flywheel energy E, energy fluctuations ΔE, position quadrature X and the mutual information $I(S:F)$ between spin and flywheel.

rameters. As a result, only the first few cycles feature a linear growth of β and $\bar{n}$. Nevertheless, our simple analytical estimate for the energy fluctuations turns out to be a rather good approximation even after many cycles, as discussed below.

D. Master equation simulations

We now describe a master equation that describes the effect of finite isochore duration. This model is used to generate the theoretical plots in Fig. 4 of the main text. The dynamics of the system is now described by a continuous evolution equation

$$\frac{\mathrm{d}\hat{\rho}}{\mathrm{d}t} = \frac{1}{\mathrm{i}\hbar}[\hat{H},\hat{\rho}] + R_+(t)\mathcal{D}[\hat{\sigma}_+]\hat{\rho} + R_-(t)\mathcal{D}[\hat{\sigma_-}]\hat{\rho}, \qquad (29)$$

where $\mathcal{D}[\hat{L}]\hat{\rho} = \hat{L}\hat{\rho}\hat{L}^\dagger - \frac{1}{2}\{\hat{L}^\dagger\hat{L}\hat{\rho}\}$ is a Lindblad dissipator and the rates $R_\pm(t) = R_\pm^{h,c}$ only take finite values during the isochores and are zero otherwise. In particular, we take $R_+(t) = R_+$ and $R_-(t) = 0$ during the hot isochore, while $R_-(t) = R_-$ and $R_+(t) = 0$ during the cold isochore. The rates are chosen to ensure that the dissipation drives the spin to an equilibrium state with the correct spin populations. In particular, we have

$$R_+ = t_h^{-1}\ln(p_\uparrow^h/p_\uparrow^c), \qquad (30)$$

$$R_- = t_c^{-1}\ln(p_\downarrow^h/p_\downarrow^c), \qquad (31)$$

where $p_{\downarrow,\uparrow}^{c,h}$ are the equilibrium probabilities of the two spin states at temperature $T_{c,h}$ and $t_{c,h}$ are the corresponding isochore durations. Note that this model is equivalent to the random-walk description of the flywheel, specifically Eq. (18), in the limit $t_{c,h} \to 0$.

Since the dissipators do not generate spin coherences, we may restrict our attention to block-diagonal solutions of Eq. (29) with the general form

$$\hat{\rho} = p_\downarrow\hat{\Pi}_\downarrow \otimes \hat{\rho}_\downarrow + p_\uparrow\hat{\Pi}_\uparrow \otimes \hat{\rho}_\uparrow, \qquad (32)$$

where $\hat{\rho}_s$ is the state of the flywheel conditioned on the spin. This indicates in particular that there are no quantum correlations between spin and flywheel. Classical correlations remain small as indicated in Fig. 4, where solutions of Eq. (29) for some pertinent observables are displayed.

In Fig. 5, the predictions of the random walk model for energy, ergotropy and relative energy fluctuations are compared with the results of the master equation. We see that the linearized approximation (20), which assumes $k_{\rm SW}\langle\hat{x}\rangle \ll 1$, breaks down after only about five engine cycles, when considering the energy and ergotropy of the flywheel. The linear approximation describes the relative energy fluctuations surprisingly well, however, even for longer times. The more accurate random-walk model (18) that includes the non-linear standing-wave potential agrees well with the master-equation predictions at all times. The finite duration of the isochores causes a small reduction in both the energy and ergotropy transferred to the flywheel, as well as a reduction in its relative energy fluctuations.

E. Estimating the effect of photon recoils

In this section we estimate the heating effect of motional recoil during optical pumping, which is neglected in Eq. (29). Circularly polarized photons absorbed from the applied laser field are spontaneously emitted with either the same polarization (Rayleigh scattering) or with linear polarization (Raman scattering). Raman scattering events lead to a change in spin state, while Rayleigh scattering events do not. In either case, the emission of a photon with wavevector $\mathbf{k}$ implies a recoil momentum $-\hbar\mathbf{k}$ acquired by the atomic centre of mass. In the following, these considerations are formalised into a simple phenomenological master equation.

In the spirit of the quantum-jump approach [10], every distinguishable change in the electromagnetic environment that may *in principle* be measured is identified with a distinct dissipation channel acting on the spin-flywheel system. We thus imagine a fictitious scenario in which the spontaneously emitted photons are detected with unit efficiency and perfect angular resolution, in a manner that distinguishes the two possible polarisation states. Suppose that the temporal resolution of the photodetectors, Δt, is much smaller than any relevant time scale of the heat engine dynamics. According to standard quantum measurement theory, the state of the heat engine after each time interval Δt updates according to a positive operator-valued measure. The physical state describing the experiment is obtained by averaging over

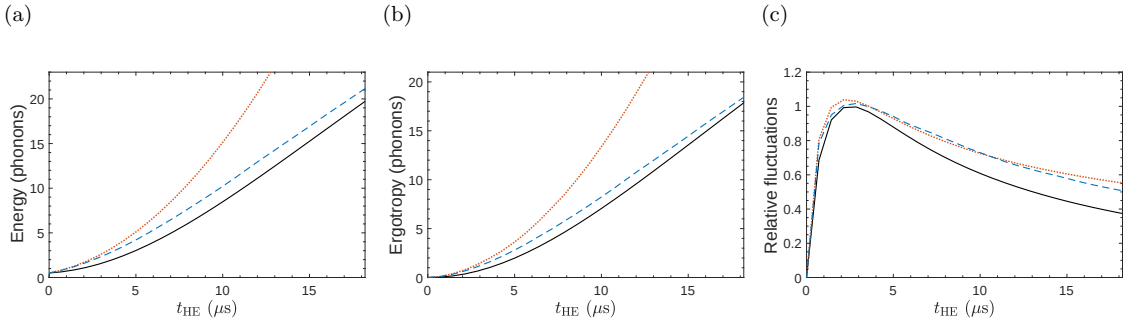


FIG. 5. Comparison between the master equation (29) (black solid line), the random-walk model (18) (blue dashed line) and its linearized approximation (23) (red dotted line) for (a) energy, (b), ergotropy and (c) relative energy fluctuations. For a fair comparison, the initial flywheel state is taken to be the vacuum state in each case.

the fictitious measurement outcomes, viz.

$$\hat{\rho}(t+\Delta t) = \hat{M}_0\hat{\rho}(t)\hat{M}_0^\dagger + \int \mathrm{d}^2\mathbf{n} \sum_{s=1}^{2} \hat{M}_s(\mathbf{n})\hat{\rho}(t)\hat{M}_s^\dagger(\mathbf{n}). \tag{33}$$

The Kraus operators $\hat{M}_s(\mathbf{n})$ describe the detection of a photon with wavevector $\mathbf{k} = 2\pi\mathbf{n}/\lambda$, with $\lambda \approx 397$ nm the resonant wavelength, and polarisation $s = 1, 2$ corresponding to Raman and Rayleigh scattering, respectively. The element of solid angle is denoted by $\mathrm{d}^2\mathbf{n} = \sin\theta \mathrm{d}\theta\mathrm{d}\phi$.

The Kraus operators are chosen to give the correct probability $\mathrm{Tr}[\hat{M}_s^\dagger(\mathbf{n})\hat{M}_s(\mathbf{n})\hat{\rho}(t)]$ and the appropriate post-selected (unnormalized) state $\hat{M}_s(\mathbf{n})\hat{\rho}(t)\hat{M}_s^\dagger(\mathbf{n})$ associated with each detectable scattering event. For example, during the hot isochore we have

$$\hat{M}_1(\mathbf{n}) = \sqrt{\Delta t R_+ f(\mathbf{n})}\hat{\sigma}_+\hat{D}(-\mathrm{i}\eta\cos\theta), \tag{34}$$

$$\hat{M}_2(\mathbf{n}) = \sqrt{2\Delta t R_+ f(\mathbf{n})}\hat{\sigma}_-\hat{\sigma}_+\hat{D}(-\mathrm{i}\eta\cos\theta), \tag{35}$$

where $f(\mathbf{n})$ is the normalized angular distribution for the outgoing photons, $\hat{D}$ is the displacement operator (10), $\eta = 2\pi x_0/\lambda$ is the Lamb-Dicke parameter and θ is the angle subtended by $\mathbf{n}$ from the motional axis of the trapped ion. The corresponding Kraus operators for the cold isochore are obtained by substituting $R_+ \to R_-$ and exchanging $\sigma_+ \leftrightarrow \sigma_-$. Here we account for the fact that the total rate of spin population transfer is equal to $R_\pm$, while the rate of Rayleigh scattering events is precisely twice that of Raman events. We have also assumed for simplicity that the angular distributions $f(\mathbf{n})$ are identical for each scattering process. Finally, the free (no detection) evolution is described by $\hat{M}_0 = \mathrm{e}^{-\mathrm{i}\Delta t\hat{H}_{\rm eff}}$, with

$$\hat{H}_{\rm eff} = \hat{H} - \frac{\mathrm{i}}{2}\int \mathrm{d}^2\mathbf{n} \sum_{s=1,2} \hat{M}_s^\dagger(\mathbf{n})\hat{M}_s(\mathbf{n}), \tag{36}$$

where the anti-Hermitian part ensures overall probability conservation at first order in Δt.

Putting this all together and expanding Eq. (33) to first order in Δt, we obtain

$$\begin{aligned}\frac{\mathrm{d}\hat{\rho}}{\mathrm{d}t} &\approx \frac{\hat{\rho}(t+\Delta t) - \hat{\rho}(t)}{\Delta t} \\ &= \frac{1}{\mathrm{i}\hbar}[\hat{H},\hat{\rho}] + R_+(t)\int_{-1}^{1}\mathrm{d}u\,\bar{f}(u)\mathcal{D}[\hat{\sigma}_+\hat{D}(-\mathrm{i}\eta u)]\hat{\rho} \\ &\quad + R_-(t)\int_{-1}^{1}\mathrm{d}u\,\bar{f}(u)\mathcal{D}[\hat{\sigma}_-\hat{D}(-\mathrm{i}\eta u)]\hat{\rho} \\ &\quad + 2R_+(t)\int_{-1}^{1}\mathrm{d}u\,\bar{f}(u)\mathcal{D}[\hat{\sigma}_-\hat{\sigma}_+\hat{D}(-\mathrm{i}\eta u)]\hat{\rho} \\ &\quad + 2R_-(t)\int_{-1}^{1}\mathrm{d}u\,\bar{f}(u)\mathcal{D}[\hat{\sigma}_+\hat{\sigma}_-\hat{D}(-\mathrm{i}\eta u)]\hat{\rho}. \end{aligned} \tag{37}$$

Here, we defined the angular distribution averaged over the azimuthal angle

$$\bar{f}(u) = \int_0^{2\pi}\mathrm{d}\phi\, f(\mathbf{n}), \tag{38}$$

where $u = \cos\theta$, the projection of $\mathbf{n}$ onto the motional axis, is held fixed.

In order to estimate the impact of photon recoil, we simulate Eq. (37) taking a simple isotropic distribution of emitted photons, $\bar{f}(u) = 1/2$, and evaluating the integrals over u on a grid of 100 evenly spaced points. In Fig. 6 we show the difference between the cycle-averaged energy

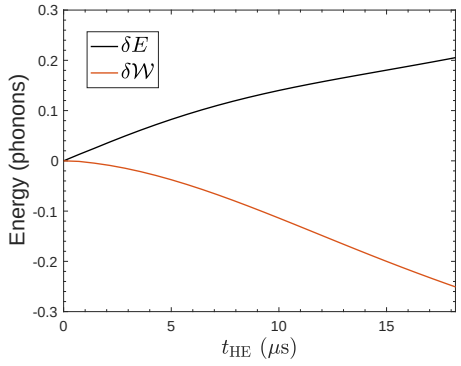


FIG. 6. Difference between energy and ergotropy computed from the master equation with and without the effect of photon recoil.

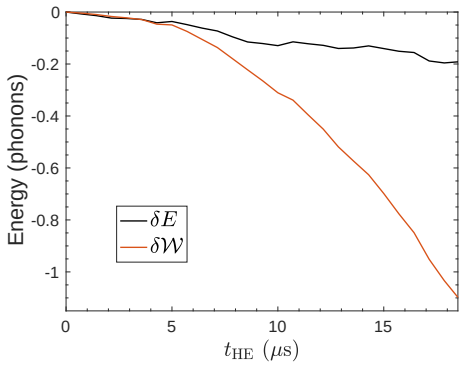


FIG. 7. Difference between energy and ergotropy computed from the random-walk model with and without the effect of SW phase jitter. The results are averaged over 10^5 random-walk trajectories.

and ergotropy as computed with and without the effect of photon recoil. As expected, photon recoil increases the energy and decreases the ergotropy by a small amount.

F. Estimating the effect of standing-wave phase jitter

In this section we estimate the effect of phase fluctuations of the standing-wave (SW) potential. In particular, we now allow for a random phase ϕ in the spin-dependent SW potential:

$$V(\hat{x}) = \pm\frac{\hbar\Delta_S}{2}\sin(k_{\mathrm{SW}}\hat{x} + \phi). \tag{39}$$

The phase drift of the SW has been measured to be $\mathrm{d}\phi/\mathrm{d}t \lesssim 0.03\pi/\mathrm{s}$ [2], which is completely negligible on the 18 μs timescale of the experiment. We thus focus on shot-to-shot fluctuations of the phase between each run of the experiment, which are equivalent to a root-mean-square position fluctuation of the trap minimum relative to the SW node of approximately 6.5 nm [2].

To estimate the effect of these fluctuations, we simulate the random-walk model given by Eq. (18) with each stochastic trajectory calculated using a different phase in the SW potential. In particular, the position of the standing-wave node relative to the trap potential minimum is shifted by a random Gaussian variable with zero mean and standard deviation 6.5 nm. As shown in Fig. 7, phase fluctuations lead to a small decrease in both the ergotropy and the energy, as compared to the random-walk model without SW phase fluctuations.

[1] A. Walther, F. Ziesel, T. Ruster, S. T. Dawkins, K. Ott, M. Hettrich, K. Singer, F. Schmidt-Kaler, and U. G. Poschinger, Phys. Rev. Lett. **109**, 080501 (2012).
[2] C. T. Schmiegelow, H. Kaufmann, T. Ruster, J. Schulz, V. Kaushal, M. Hettrich, F. Schmidt-Kaler, and U. G. Poschinger, Phys. Rev. Lett. **116**, 033002 (2016).
[3] F. Ziesel, T. Ruster, A. Walther, H. Kaufmann, S. Dawkins, K. Singer, F. Schmidt-Kaler, and U. Poschinger, J. Phys. B: At. Mol. Opt. Phys. **46**, 104008 (2013).
[4] U. Poschinger, G. Huber, F. Ziesel, M. Deiss, M. Hettrich, S. Schulz, G. Poulsen, M. Drewsen, R. Hendricks, K. Singer, and F. Schmidt-Kaler, J. Phys. B: At. Mol. Opt. Phys. **42**, 154013 (2009).
[5] A. Allahverdyan, R. Balian, and T. M. Nieuwenhuizen, EPL **67**, 565 (2004).
[6] W. Pusz and S. L. Woronowicz, Communications in Mathematical Physics **58**, 273 (1978).
[7] A. Lenard, Journal of Statistical Physics **19**, 575 (1978).
[8] F. Binder, S. Vinjanampathy, K. Modi, and J. Goold, Physical Review E **91**, 032119 (2015).
[9] G. Francica, J. Goold, F. Plastina, and M. Paternostro, npj Quantum Information **3**, 12 (2017).
[10] M. B. Plenio and P. L. Knight, Rev. Mod. Phys. **70**, 101 (1998).